Available online at www.sciencedirect.com
ScienceDirect
Journal of the European Ceramic Society 28 (2008) 49–60
www.elsevier.com/locate/jeurceramsoc

Solid-state dewetting of $La_{0.6}Sr_{0.4}Co_{0.2}Fe_{0.8}O_{3\pm\delta}$ thin films during annealing

Daniel Beckel [a,*], Alban Dubach [b], A. Nicholas Grundy [c], Anna Infortuna [a], Ludwig J. Gauckler [a]

[a] *Nonmetallic Inorganic Materials, Department of Materials, ETH Zürich, CH-8093 Zürich, Switzerland*
[b] *Metal Physics and Technology, Department of Materials, ETH Zürich, CH-8093 Zürich, Switzerland*
[c] *Centre de Recherche en Calcul Thermodynamique, École Polytechnique de Montréal, Montréal, Québec H3C 3A7, Canada*

Received 10 February 2007; received in revised form 26 April 2007; accepted 5 May 2007
Available online 20 July 2007

Abstract

Porous $La_{0.6}Sr_{0.4}Co_{0.2}Fe_{0.8}O_{3\pm\delta}$ (LSCF) thin film cathodes were fabricated by spray pyrolysis and pulsed laser deposition (PLD). These films show nanometer sized grains and a thickness <1 μm. They are dense after deposition and develop porosity upon annealing at 600–900 °C. Sprayed films develop roughly twice the porosity of films deposited by PLD. Solid-state dewetting similar to metallic films is proposed as the mechanism for the pore formation. The amount of porosity can be tailored by the deposition process, the annealing conditions and the chemistry of the precursor. The connection between porosity and electrical conductivity was also investigated.

Keywords: Porosity; Microstructure-final; Films; Perovskites; Grain size; (La,Sr)(Co,Fe)O_3

1. Introduction

Porous thin films are of great importance for many chemical and electrochemical applications such as electronic devices, sensors, catalysts and electrodes. The material investigated in the current work, $La_{0.6}Sr_{0.4}Co_{0.2}Fe_{0.8}O_{3\pm\delta}$ (LSCF), is used as a cathode in solid oxide fuel cells (SOFCs). SOFCs are used for efficient conversion of chemical into electrical energy at high (800–1000 °C) temperatures. The cathode has to provide a large solid–gas interface for oxygen reduction, thus a porous microstructure is desirable. For large, thick-film-based state-of-the-art fuel cells, cathodes (20–50 μm thick) are fabricated by spraying suspensions and pastes, or by screen printing or tape casting.[1–5] The required microstructure is achieved by the use of pore formers that are burned out to create porosity.

In order to reduce material degradation, SOFC research aims to reduce the operating temperature to 500–700 °C. The increase of resistivity associated with the lowered operating temperature is compensated for by the use of thin films (some 100 nm thick). In this way the ohmic resistance of the cell is kept low by geometrical means.[6] Therefore tape casting or screen printing have to be replaced by thin film deposition techniques,[7] e.g. spray pyrolysis or pulsed laser deposition (PLD). The use of thin films also enables the fabrication of micro-SOFCs,[8–10] which leads to new applications for SOFCs, such as battery replacement for portable devices.

In this paper we investigate the preparation of porous LSCF thin film cathodes, which were prepared without the aid of a pore former, by spray pyrolysis and PLD and discuss their microstructural evolution during post-deposition annealing. Different means to tailor the porosity are also presented.

2. Experimental

The thin films were deposited onto different substrates. Afterwards, they were annealed in air for specific times at specific temperatures and the microstructure and the crystalline phase were analyzed. The details of each step are given in the following sections.

2.1. Thin film deposition

Air-pressurized spray pyrolysis[11–17] and PLD[18,19] were used for the deposition of the thin films.

2.1.1. Spray pyrolysis

Details of the experimental setup can be found elsewhere.[11] Nitrates and chlorides were used as metal salts to prepare the

* Corresponding author. Tel.: +41 44 632 3763; fax: +41 44 632 1132.
E-mail address: Daniel.Beckel@mat.ethz.ch (D. Beckel).

0955-2219/$ – see front matter © 2007 Elsevier Ltd. All rights reserved.
doi:10.1016/j.jeurceramsoc.2007.05.004

spray solution. Specifically, $La(NO_3)_3{\cdot}6H_2O$ (ABCR purity > 99%), $LaCl_3{\cdot}7H_2O$ (Alfa Aesar), $SrCl_2{\cdot}6H_2O$ (Fluka > 99%), $Sr(NO_3)_2$ (Fluka > 99%), $Co(NO_3)_2{\cdot}6H_2O$ (Alfa Aesar and Fluka > 98%), $Fe(NO_3)_3{\cdot}9H_2O$ (Fluka > 98%), $FeCl_3{\cdot}6H_2O$ (Fluka > 98%) were used. As solvent a mixture of 1/3 (vol. fraction) ethanol (Scharlau and Merck, >99.5%) and 2/3 diethylene glycol monobutyl ether (Acros Organic > 99%) was used. Unless otherwise noted, nitrates were used for preparation of the spray solutions except for Sr, where the chloride was used. The total salt concentration was 0.02 or 0.04 mol/l. The deposition time was 45 min for 0.04 mol/l salt concentration and twice the time for half the salt concentration. The flow rate of the spray solution was 30 ml/h. These conditions resulted in a film thickness of about 600 nm. For atomization of the solution, an air pressure of 1 bar was used. The obtained droplets were sprayed onto the heated substrate where an amorphous metal oxide film was formed.

The substrate surface temperature was 280 °C for sapphire single crystal (Stettler, Lyss, Switzerland (1 1 $\bar{2}$ 0) orientation parallel to the surface) and polycrystalline aluminum oxide (alox) substrates and 255 °C for Si substrates ((1 0 0) single crystal, Prolog Semicor, Kiev, Ukraine). A thin native oxide layer for the latter due to the processing at elevated temperatures is to be expected. The substrate surface temperature was measured with a type K surface probe (Omega Model 88108). The difference in substrate temperature was to account for the difference in heat transfer from the substrate to the arriving droplet.[13] Si and sapphire substrates were used for X-ray diffraction (XRD) characterization; for conductivity measurements sapphire was used as substrate. Alox substrates were used for microstructure characterization of the sprayed films.

For the conductivity measurements, the thin films were deposited through a shadow mask (200 μm thick laser-cut molybdenum) to achieve a defined film geometry as illustrated in Fig. 1(A)–(C).

Crystallization was carried out in a separate annealing step in air; details of the annealing temperature and time are given in Section 3.

2.1.2. Pulsed laser deposition

The target for PLD (PLD workstation, Surface, Hueckelhoven, Germany) was uniaxially (7 MPa, 100 s) and isostatically (256 MPa, 3 min) pressed from LSCF powder (Praxair, Danbury, CT, USA >99.9%) and sintered for 4 h at 1250 °C in air with a heating rate of 3 °C/min and a cooling rate of 5 °C/min. More details on the pressing procedure can be found in the cited reference.[6] The Si substrate ((1 0 0) single crystal with native oxide layer, University Wafers) on which the films were deposited was placed at a distance of 6.5 cm from the target. A 248 nm excimer laser with 4 J/cm^2 fluence was used with 0.26 mbar oxygen pressure in the deposition chamber. The substrate temperature was 400 °C. Fifty thousand pulses at a rate of 10 Hz were used to form 400 nm thick films.

2.2. Porosity and grain size characterization

Scanning electron microscope (SEM) images were obtained with a Leo 1530 (Carl Zeiss SMT). Images were taken with the in-lens detector using 5 kV acceleration voltage. The grain size and the porosity were determined from SEM images by quantitative image analysis using the software Lince.[20]

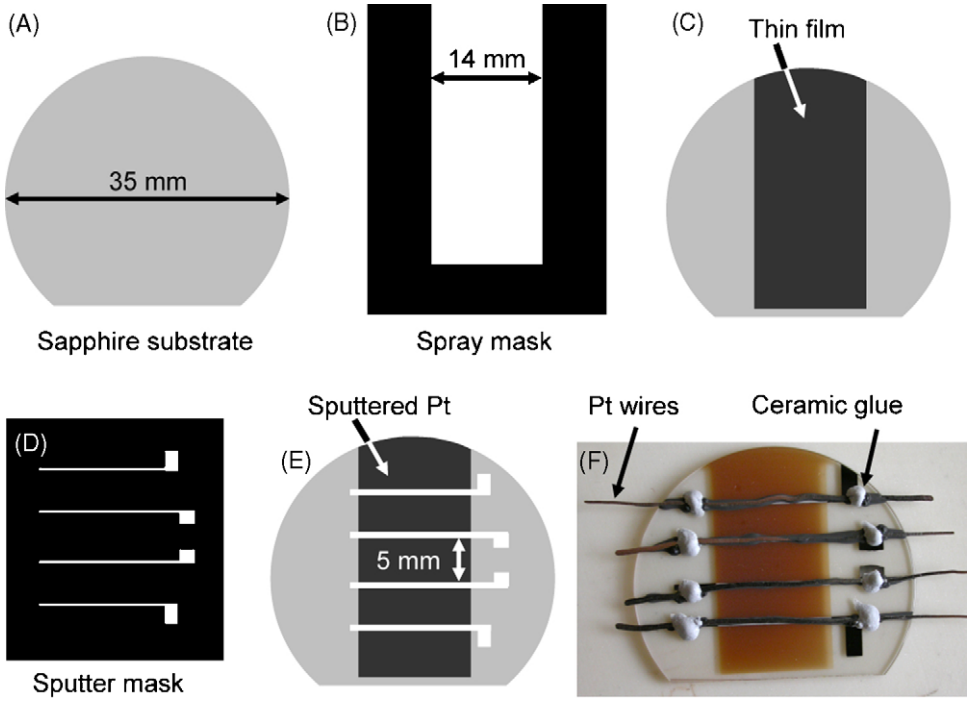

Fig. 1. Sketch of sample contacting: (A) sapphire substrate, (B) spray mask to define film geometry, (C) thin film on sapphire, (D) mask for sputtering the Pt contacts (E). (F) Picture of a fully contacted sample with Pt wires attached with Pt paste and ceramic glue to the sputtered Pt and the substrate, respectively.

2.3. X-ray diffraction

The crystal phases were analyzed using XRD (Siemens Diffraktometer D5000 Kristalloflex, Cu Kα radiation) on the actual thin films on silicon and sapphire substrates. The reflections of the substrates were used as calibration standard. The step size was 0.01 and the time per step 10 s.

2.4. Electrical conductivity measurements

The electrical conductivity of the thin films was measured in air using four-point measurement.[21–23] Generally, the samples were annealed prior to contacting. As electrodes, four Pt (target from Baltec) stripes each 1 mm wide were sputtered through a shadow mask (200 μm thick laser-cut molybdenum, see Fig. 1(D) and (E) at room temperature for 4 min with 60 mA

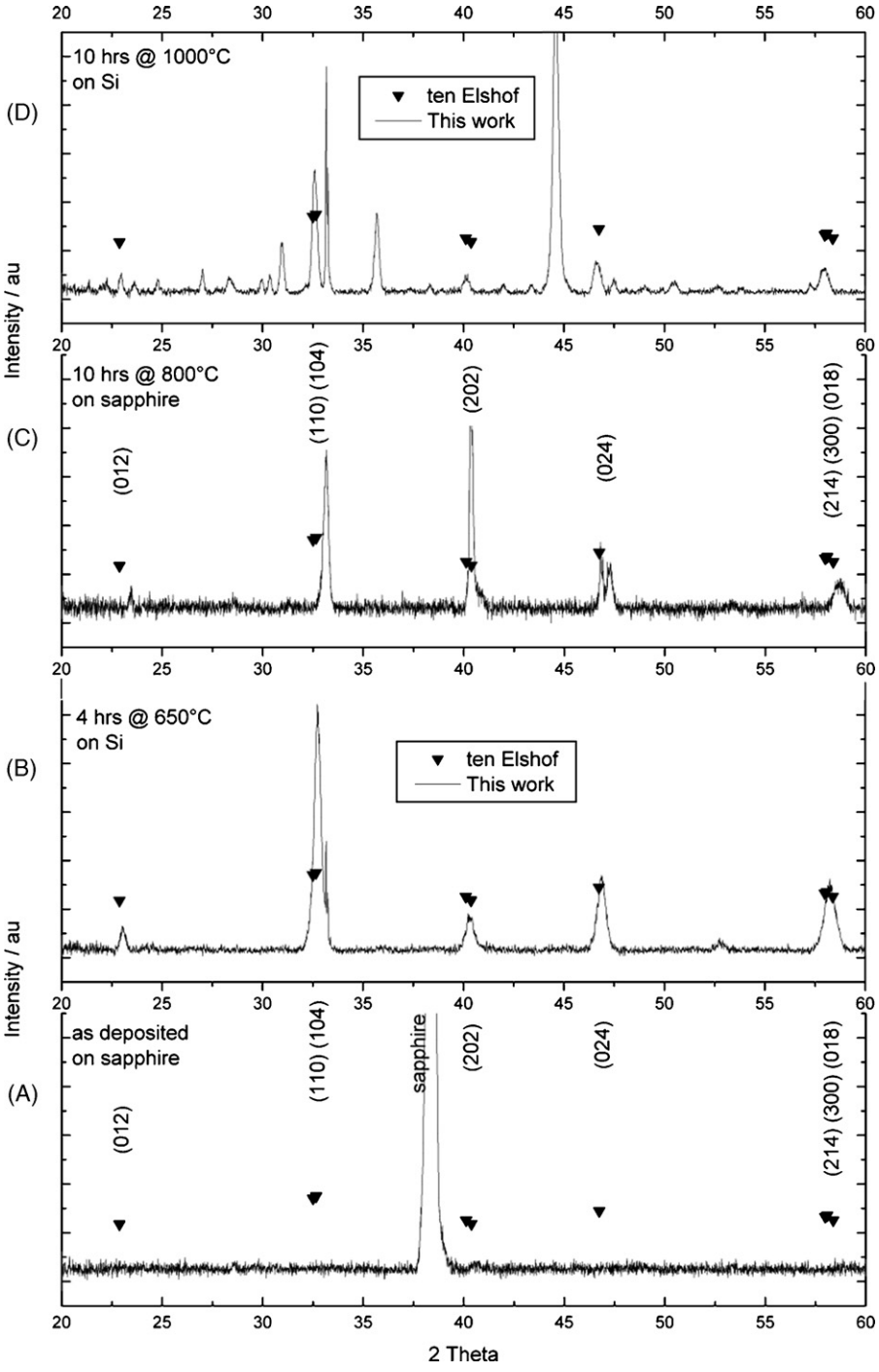

Fig. 2. XRD patterns of sprayed LSCF thin films: (A) as deposited on sapphire, (B) deposited on Si, annealed at 650 °C for 4 h, (C) 10 h at 800 °C on sapphire, (D) 10 h at 1000 °C on Si. At 1000 °C secondary phases appear. A reference for the same composition ($La_{0.6}Sr_{0.4}Co_{0.2}Fe_{0.8}O_3$ ten Elshof[25]) is also shown.

at 5×10^{-2} mbar Ar pressure and a working distance of 6 cm using a Baltec SCD 050 sputter coater. Fritless Pt paste (Heraeus C 3605 P) was painted on flat-pressed Pt wires (0.25 mm diameter, Johnson Matthey, thermocouple quality) which were then put on the four sputtered Pt stripes. As depicted in Fig. 1(F), the wires were glued to the substrate outside the film area using non-conductive ceramic glue (Firag, Ebmatingen, Switzerland, type WH 1500) mixed with some Pt powder (>99.9%, Johnson Matthey, <10 μm) to improve adhesion to the sapphire. The amount of Pt powder added to the ceramic glue was not enough to make the resulting glue conductive. After a drying step (1 h at 120 °C in air), the electrodes were spot-welded (Resistronic 3201) to Pt wires that led from the inside of a furnace to the outside where they were connected to a Multimeter (Keithley 2000). Then the samples were heated with this furnace to the target temperature (3 °C/min) and cooled again (3 °C/min). The data were recorded during the cooling ramp.

2.5. Differential thermal analysis, thermogravimetry, mass spectroscopy

Experiments to follow the decomposition reactions were carried out on material from scratched off films after spray deposition using differential thermal analysis (DTA) combined with thermogravimetry (TG, both Netzsch STA 449 C Jupiter) coupled to a mass spectrometer (MS, Balzers Thermostar). The atmosphere during investigation was 21% oxygen and 79% argon, the heating rate was 10 °C/min.

3. Results and discussion

3.1. XRD

All films investigated by XRD were deposited by spray pyrolysis onto sapphire and Si. The reason to use two different substrates was to exclude substrate-specific reactions. In Fig. 2(A), the XRD scan of an as-deposited LSCF film is shown, no distinct peaks except for the substrate (sapphire) can be found. Fig. 2(B) shows the XRD scan for a film deposited on Si and annealed at 650 °C for 4 h in air, which already results in the formation of only the desired rhombohedral perovskite. The hexagonal lattice parameters of $a = 5.51$ Å and $c = 13.51$ Å were calculated[24] and are in good agreement with literature data obtained for powder of the same stoichiometry: $a = 5.51$ Å, $c = 13.39$ Å.[25] Fig. 2(C) shows a film deposited on sapphire and annealed for 10 h at 800 °C in air. Also this film shows single phase perovskite. Here no peaks from the substrate (sapphire) were found, because the appearance of peaks from the single crystals depends on the orientation of the sample relative to the X-ray beam and on the film thickness, which could vary by about ±30%. The film shown in Fig. 2(D) is deposited on Si and annealed at 1000 °C for 10 h. In this sample the formation of unidentified secondary phases was detected. The reason for the formation of these secondary phases is not fully understood, since bulk LSCF perovskites are still stable at these temperatures.[26,27] Reactions with the substrate are possible, but no Si-containing phase could be identified with these peaks. Evaporation of Co and phase separation of the remaining oxides is also possible as it has been suggested for LSC thin films at 1000 °C.[28] However, in the temperature range

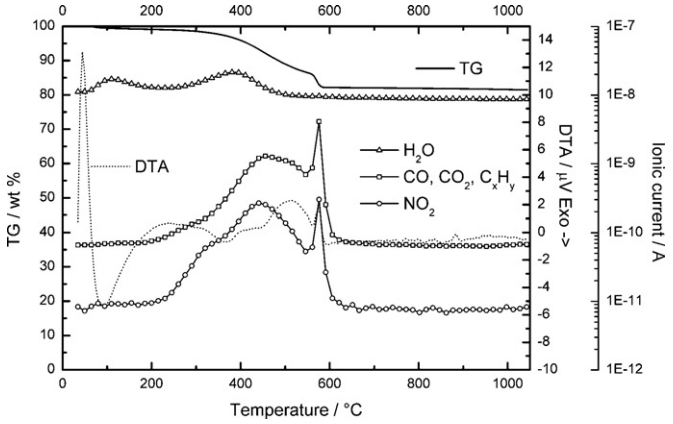

Fig. 3. DTA, TG and MS results of a film scratched off for analysis after deposition by spray pyrolysis.

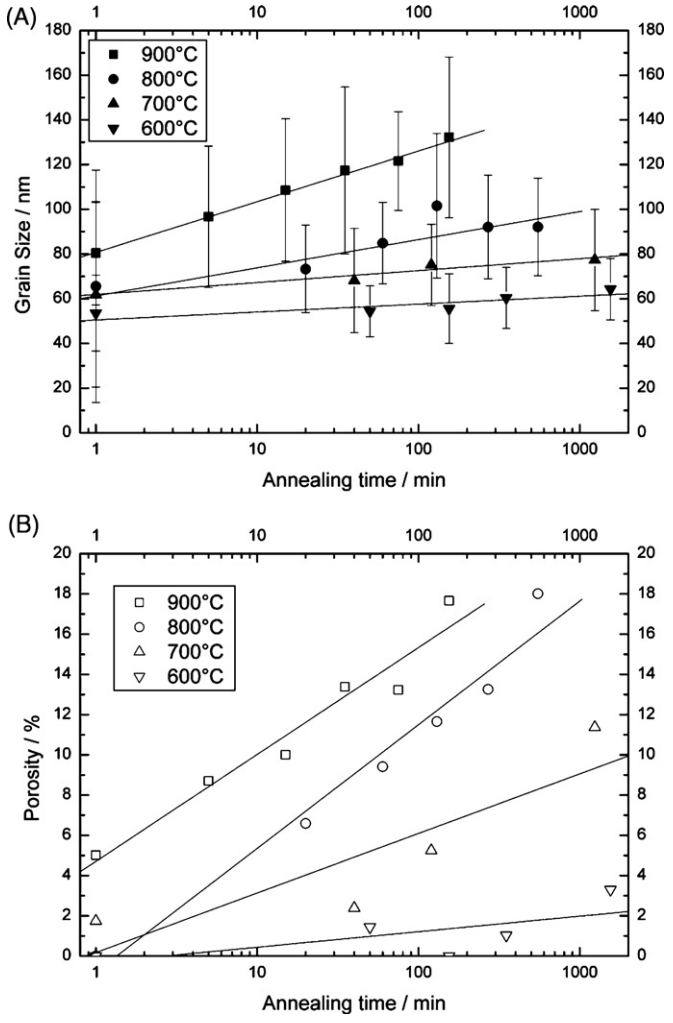

Fig. 4. Evolution of grain size (A) and porosity (B) with annealing time for different temperatures (sprayed films).

Table 1
Numerical data from the graphs in Fig. 4

Annealing temperature (°C)	Annealing time (min)	GS (nm)	Por (%)	A_{GS}	B_{GS}	A_{Por}	B_{Por}	PS (nm)
600	1	54 ± 17	0	50.50	3.54	−0.33	0.77	–
	50	54 ± 11	1.4					30 ± 10
	155	56 ± 16	0					–
	350	60 ± 14	1.0					22 ± 2.6
	1,550	65 ± 14	3.3					31 ± 8.0
	601,782	79 ± 21	7.8	–	–	–	–	29 ± 10
700	1	62 ± 41	1.7	61.91	5.33	0.17	2.96	33 ± 8.3
	40	68 ± 23	2.4					23 ± 3.0
	120	77 ± 19	5.2					28 ± 10
	1,240	77 ± 23	11.4					30 ± 11
800	1	66 ± 52	0	61.27	12.57	−0.80	6.15	–
	20	73 ± 20	6.6					33 ± 17
	60	85 ± 18	9.4					31 ± 17
	130	102 ± 32	11.7					33 ± 17
	270	92 ± 23	13.3					34 ± 14
	550	92 ± 22	18.0					43 ± 26
900	1	80 ± 23	5.0	80.70	22.68	4.71	5.31	29 ± 9.3
	5	97 ± 32	8.7					36 ± 13
	15	109 ± 32	10.0					28 ± 11
	35	117 ± 37	13.4					41 ± 21
	75	122 ± 22	13.2					35 ± 7
	155	132 ± 36	17.7					62 ± 30

GS: grain size, Por: porosity. The formulae for the fits are GS (nm) = $A_{GS} + B_{GS}$ log(t (min)) and Por (%) = $A_{Por} + B_{Por}$ log(t (min)), respectively with the constants A and B given in the table and t: annealing time. PS: pore size.

for the application of these films (<800 °C) the single perovskite phase is obtained and these additional phases are of no consequence.

3.2. DTA/TG/MS

Mass loss, heat flux and outgassing species were detected using DTA/TG/MS during heating of the film material after spray deposition. The result is shown in Fig. 3. From the deposition temperature to about 600 °C, the TG curve indicates a mass loss of 18 wt%. Additionally, all significant peaks in the DTA signal as well as the outgassing hydrocarbons and nitrate decomposition products were detected below 600 °C. Chlorides could not be detected and possibly remained in the film. Between 600 and 1000 °C the mass loss is only 0.5 wt%.

During investigation of single salts by DTA/TG/MS, no general trend, such that chloride salts generally decompose at lower or higher temperatures than nitrate salts was found.

3.3. Microstructural evolution during annealing

To characterize the microstructural evolution, the thin films were heated to the target temperature (600, 700, 800 or 900 °C) with a heating rate of 3 °C/min. The annealing time was counted after reaching the target temperature. The samples were removed from the furnace after annealing for the specified time. The microstructure was then analyzed to determine the grain size, the porosity and the pore size. For films fabricated by spray pyrolysis, the result is shown graphically in Fig. 4 and numerically in Table 1. SEM images showing the microstructure of

Table 2
Numerical data for the microstructural evolution of thin films deposited by PLD

Annealing temperature (°C)	Annealing time (min)	GS (nm)	Por (%)	A_{GS}	B_{GS}	A_{Por}	B_{Por}	PS (nm)
600	1	15 ± 5	0	14.71	12.12	−0.52	0.82	–
	60	35 ± 13	0					–
	240	48 ± 17	1.3					29 ± 6.0
	2880	55 ± 16	2.9					15 ± 5.0
800	1	20 ± 5	2.1	18.33	23.83	2.10	1.17	9.2 ± 2.6
	60	39 ± 11	4.0					15 ± 4.8
	240	119 ± 38	4.4					58 ± 17
	480	144 ± 38	6.3					62 ± 26
	1440	147 ± 38	7.6					67 ± 24
	2880	156 ± 64	4.7					58 ± 20

GS: grain size; Por: porosity. The formulae for the fits are GS (nm) = $A_{GS} + B_{GS}$ log(t (min)) and Por (%) = $A_{Por} + B_{Por}$ log(t (min)), respectively with the constants A and B given in the table and t: annealing time. PS: pore size.

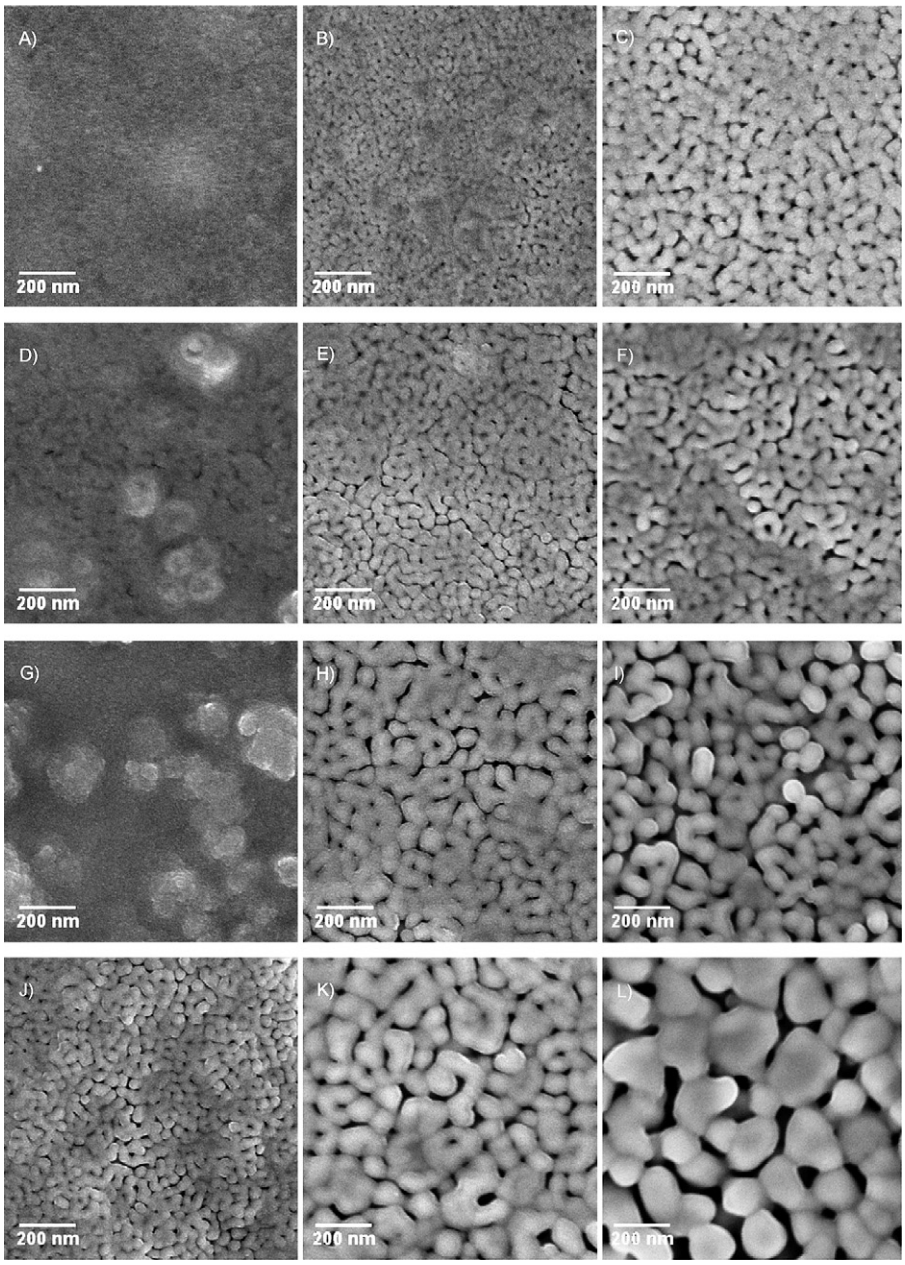

Fig. 5. SEM images of the evolving microstructure with annealing time for different temperatures (sprayed films)—first row, 600 °C: (A) 1 min, (B) 1550 min, (C) 601,782 min. Second row, 700 °C: (D) 1 min, (E) 120 min, (F) 1240 min. Third row, 800 °C: (G) 1 min, (H) 60 min, (I) 550 min. Fourth row, 900 °C: (J) 1 min, (K) 35 min and (L) 155 min.

some samples are shown in Fig. 5. For films prepared by PLD the numerical data is given in Table 2 and representative microstructures are shown in Fig. 6. Fig. 7 shows cross-section images of the films and reveals that the pores are not restricted to the film surface but are distributed over the entire cross-section.

Grain sizes and porosity increase with annealing time for all annealing temperatures. Increasing annealing temperature proves to be more effective than increasing the annealing time to obtain larger grains and higher porosity. Linear fits for the grain size and the porosity versus logarithmic annealing time according to

$$\mathrm{GS} = A_{\mathrm{GS}} + B_{\mathrm{GS}} \log(t) \quad \text{and} \quad \mathrm{Por} = A_{\mathrm{Por}} + B_{\mathrm{Por}} \log(t) \qquad (1)$$

are also included in the tables and graphically shown for the sprayed films in Fig. 4. In these equations, GS is the grain size in nm, A_{GS}, A_{Por}, B_{GS}, B_{Por} are constants, t is the annealing time in min and Por is the porosity in %. These formulae were chosen since they give a good fit to the data. It is well known[29] that grain growth laws derived for dense material[30,31] do not give a reasonable fit for the grain growth in porous material.

The slope (B) of the linear fit for the grain sizes increases from 3.5 to 22.7 when raising the annealing temperature from 600 to 900 °C, for the sprayed films and from 12.1 (600 °C) to 23.8 (800 °C) for the films deposited by PLD. The steeper slopes for the films prepared by PLD are mainly due to the very small grain sizes at the beginning of the annealing. At 600 °C anneal-

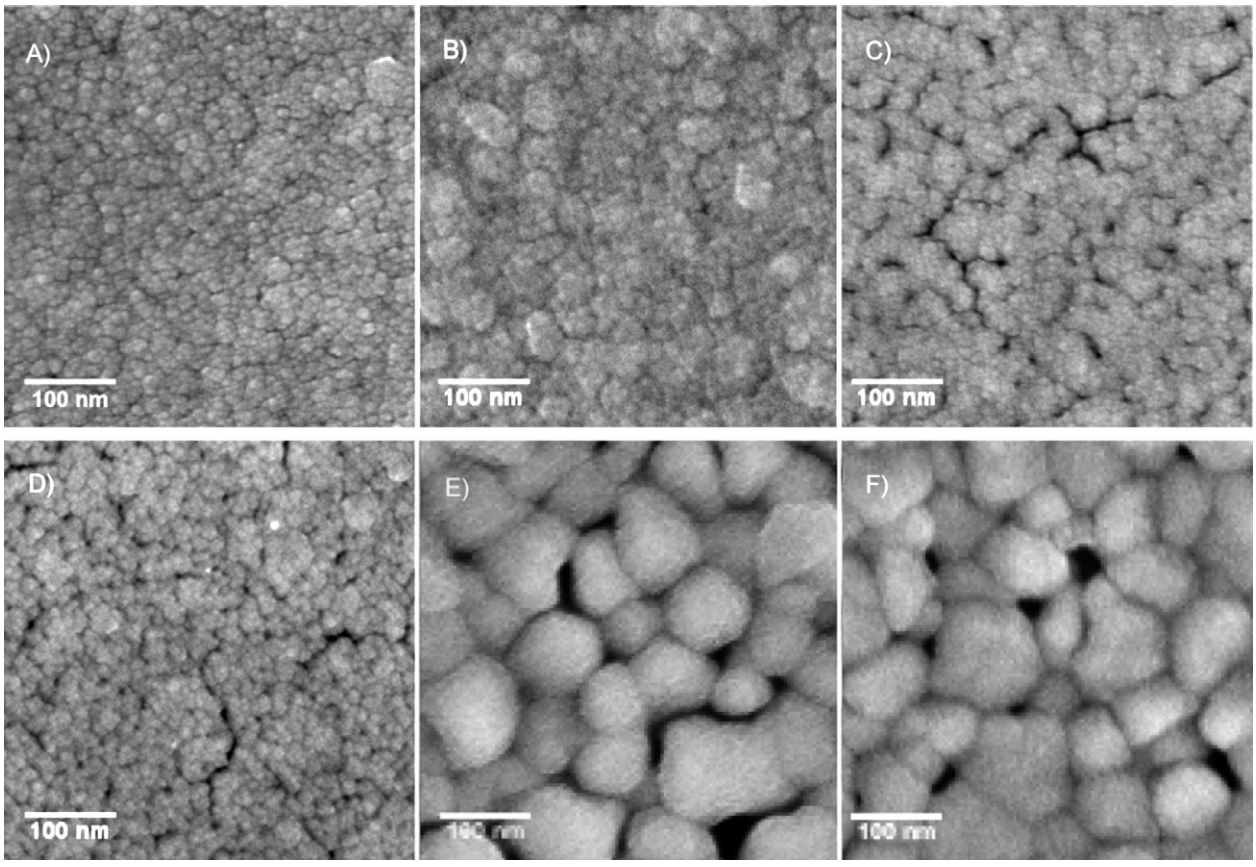

Fig. 6. SEM images of the evolving microstructure with annealing time for different temperatures (films prepared by PLD)—first row, 600 °C: (A) 1 min, (B) 60 min, (C) 2880 min. Second row, 800 °C: (D) 1 min, (E) 480 min, (F) 2880 min.

ing temperature, the grain size of the samples prepared by PLD was always smaller than the grain size of the sprayed samples for comparable annealing times. However, at an annealing temperature of 800 °C this was only the case for shorter annealing times below ∼4 h. For longer annealing times the grains in a film prepared by PLD grow faster. The smaller initial grain size of films prepared by PLD might be correlated with the columnar structure of the grains as shown in Fig. 7(L)–(O). The grain size analysis was done with top view images, so the widths and not the lengths of the columns are represented in the grain size plots. The reason for the stronger grain growth in PLD films than in sprayed films for long annealing times at 800 °C is less obvious. It can be noted that it correlates very roughly with the time at which the porosity becomes noticeable in films prepared by PLD. However, since the sprayed films always show higher porosity than the films prepared by PLD, the reason for this behavior is not yet fully clarified.

For the porosity of the sprayed films, the slope of the linear fit increases from 0.8 to 6.1 when raising the annealing temperature from 600 to 800 °C. The slope for the samples annealed at 900 °C is 5.3. For the films prepared by PLD the slope for the linear fit to the porosity evolution increases from 0.8 (600 °C) to 1.2 (800 °C). Thus the porosity increase (and also the amount of porosity) is comparable for low temperatures for both types of films. However, at higher temperatures sprayed films develop porosity faster and always show higher porosity than films deposited by PLD.

With the linear fits, the grain size and porosity can be calculated for fixed annealing times and varying temperatures as shown in Fig. 8 for the sprayed films. Arrhenius-type activation energies for grain growth show two activation energies: for temperatures between 600 and 800 °C activation energies from 0.08 eV (1 min annealing) to 0.19 eV (1000 min annealing) are found. For the temperature range of 800–900 °C, activation energies from 0.30 eV (10 min annealing) to 0.44 eV (1000 min annealing) are found. The two different activation energies indicate that two different material transport mechanisms are dominant in the two temperature regimes. Activation energies for the increase in porosity decrease from 0.89 eV (10 min annealing) to 0.70 eV (1000 min annealing). Here no difference between the two temperatures is found. All activation energies are detailed in Table 3.

In order to check if grain growth and porosity are saturated with long annealing times a sprayed sample was annealed for more than 1 year at 600 °C. Grain growth was still observed and the grain size and porosity are close to what is expected from the linear fit for the first 1550 min, so no saturation is observed. The microstructure of this sample is shown in Fig. 5(C) and the data are also included in Table 1.

Generally, the pore size also increases with annealing time and temperature. However the scattering of the data is more pronounced than for the grain growth. This can be attributed to the larger pore size distribution, which is caused by the irregular

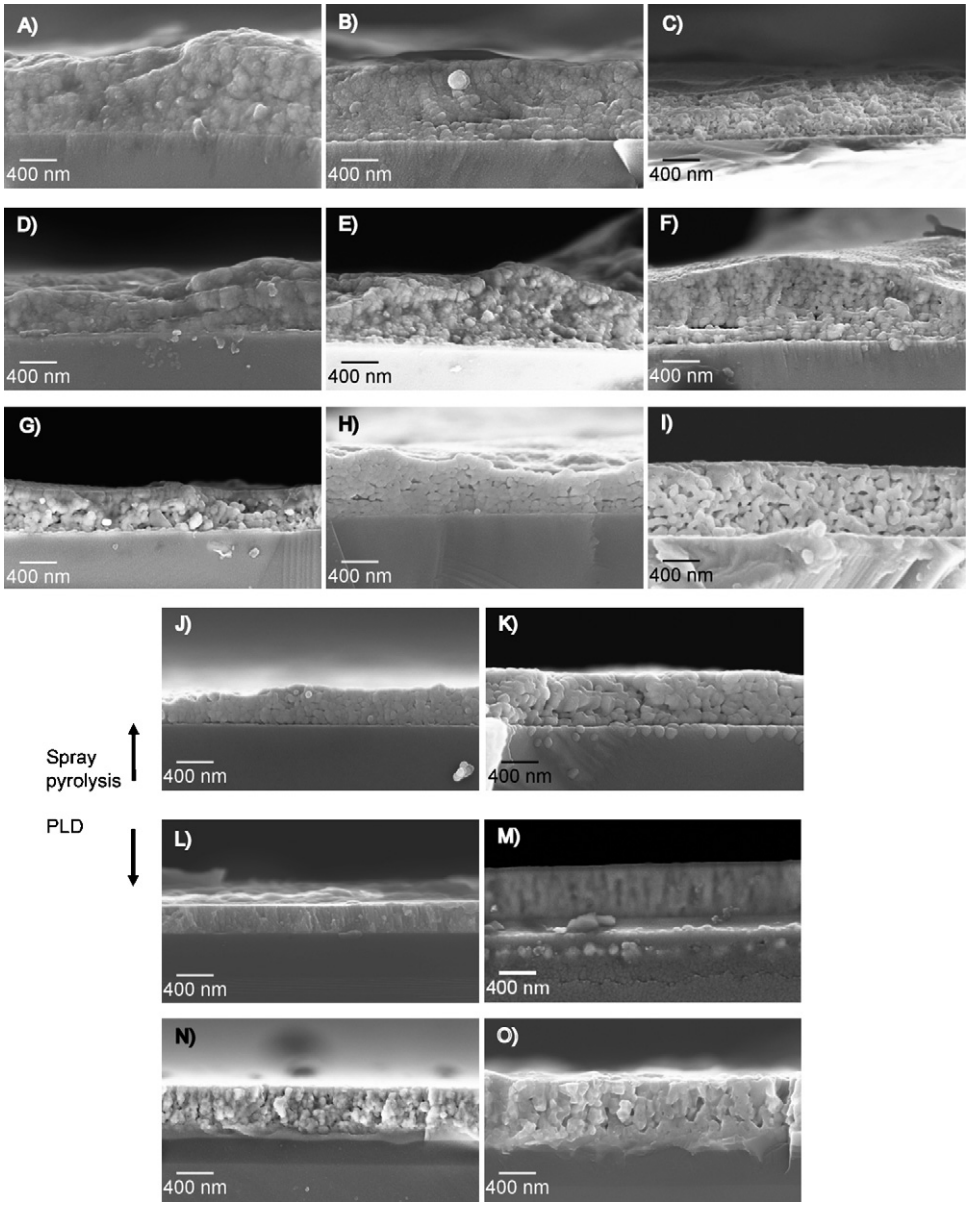

Fig. 7. SEM cross-sections of films deposited by spray pyrolysis (A)–(K) and PLD (L)–(O). Films were annealed at different temperatures for varying times. First row, 600 °C: (A) 1 min, (B) 155 min, (C) 601782 min. Second row, 700 °C: (D) 1 min, (E) 40 min, (F) 120 min. Third row, 800 °C: (G) 20 min, (H) 60 min, (I) 550 min. Fourth row, 900 °C: (J) 1 min, (K) 35 min. Fifth row, 600 °C: (L) 60 min, (M) 1440 min. Sixth row, 800 °C: (N) 240 min, (O) 480 min.

shape of the pores, e.g. the length of some pores is more than five times their width.

In a previous study for $Ce_{0.8}Gd_{0.2}O_{1.9}$ (CGO) thin films that were also produced by spray pyrolysis[15] we found limiting grain growth for long annealing times and no porosity being formed. Here, in contrast to these findings, we do not observe a limiting grain growth for LSCF although our study was carried out for the same annealing times and temperatures. However, in contrast to CGO, the LSCF grains are 2–5 times larger and, more important, while the CGO films were found to be dense and remained dense during annealing, the originally dense LSCF films developed porosity during annealing in parallel with grain growth.

Table 3
Activation energies (A_E) for grain growth (GS) and porosity (Por) increase

	$A_{E,GS}$ (eV)				$A_{E,Por}$ (eV)		
600 °C ≤ T ≤ 800 °C	0.08	0.13	0.16	0.19	0.89	0.75	0.70
800 °C ≤ T ≤ 900 °C	0.30	0.37	0.41	0.44			
t (min)	1	10	100	1000	10	100	1000

Samples prepared by spray pyrolysis. t = annealing time.

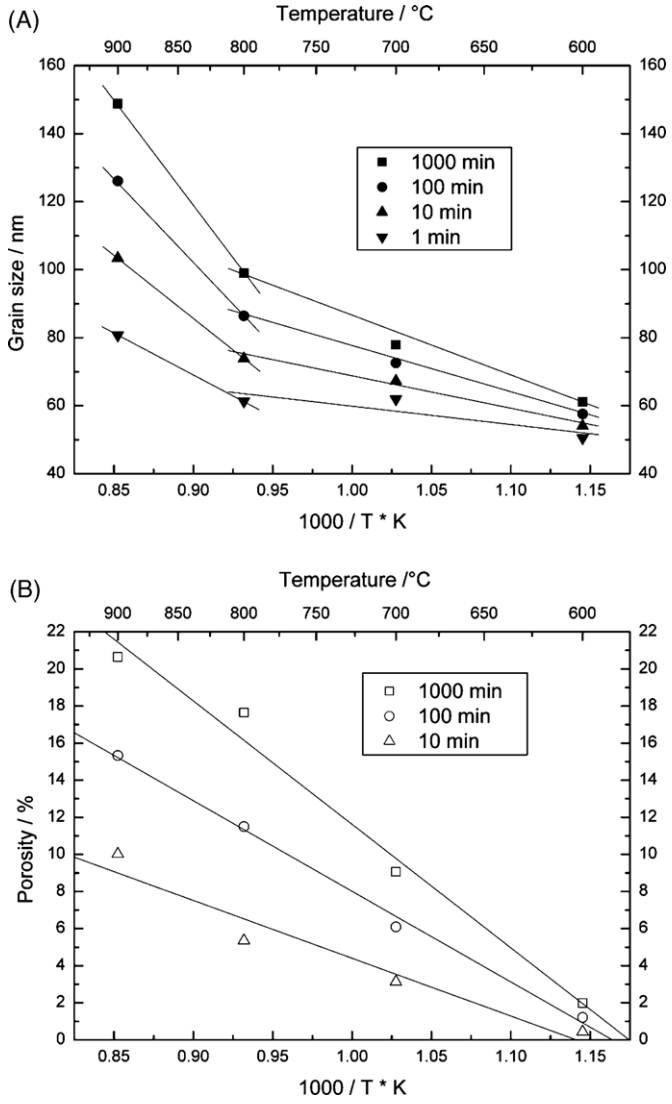

Fig. 8. Calculated grain sizes (A) and porosity (B) for different annealing times and temperatures (sprayed films).

3.4. Porosity formation due to solid-state dewetting

Annealing of granular materials is usually associated with densification of the microstructure. In contrast to this behavior, formation of porosity during annealing of solid films has been reported. It was found that thin (<30 nm) Si films on SiO_2 substrates show dewetting driven by surface energy reduction, when these films were annealed at 850 °C.[32] A similar observation was made for metal thin films (3–10 nm) such as Pt on SiO_2 substrates.[33] Here, thermally activated dewetting occurred at 620 °C due to the high energies of metal surfaces and interfaces between Si and SiO_2 ([33] and references herein).

For dense solid films, dewetting starts with the nucleation of voids on defects. Once holes are nucleated, the growth is driven by capillary forces arising from the balance of surface and interface energy.[34–38] It was demonstrated that also metal oxides such as Fe_2O_3[39] and NiO[34] in the form of thin films of 80–100 nm thickness on Si substrates show dewetting. Nucleation occurred on defects created by ion bombardment.

Similar to these observations, we assume that the developing porosity in the LSCF thin films is also a solid-state dewetting phenomenon which is related to the film and substrate materials, the preparation process and the geometry of the film. We assume the film material to be the most important parameter for this phenomenon, since we observed the porosity increase for LSCF films on every substrate tested so far (Si, alox, sapphire, stainless steel) and we observed it for different deposition methods (spray pyrolysis and PLD).

The preparation process however does have an influence on the amount of porosity found in the films. Films grown by PLD developed fewer pores than films grown by spray pyrolysis. The film preparation process is responsible for the concentration of defects created in the film, which serve as nucleation sites for the holes. Spray pyrolysis might produce a higher density of such defects than PLD due to the large mass loss during pyrolysis of the precursor as described in Section 3.2. PLD on the other hand is a solid-state process, so no evaporation of solid ceramic material at these temperatures can be expected, thus only the grain boundaries serve as defects.

The geometry could also be expected to play a role. The films are constrained on rigid substrates, thus they cannot shrink laterally. Literature describes this phenomenon as constrained sintering of thin films.[40–45] During sintering the thin film cannot densify isotropically due to the constraint, so the initial pores grow further and densification is hindered. Since not all films of the same geometry show pore development (LSCF shows porosity, CGO does not), the fixture to the substrate during annealing can only support and possibly enhance pore formation but it cannot be the main cause.

We also briefly want to discuss other mechanisms that can lead to porosity in thin films; however, we do not think that they apply here. One possibility to create porous films is through outgassing material. This can be excluded here, since outgassing is only found below the annealing temperatures and times where we find porosity as shown in Fig. 3. Similarly we can exclude a notable density change in the films. The density of the films cannot be measured by the Archimedes method since they are only about 500 nm thick and the supporting substrate is at least 600 times thicker. This means the mass of the sample is always dominated by the mass of the substrate. Consequently, the density of the amorphous films is not accessible. However, the crystallographic density can be determined for the annealed samples. Here we do not find a change in density, between dense samples (annealed for 1 min at 600 °C) and porous samples (annealed at 900 °C). If a distinct change in density resulting in porosity formation had occurred in the transition from amorphous to crystalline we would expect to see the porosity already in the samples annealed for short time at 600 °C (where we see first peaks in the XRD), which is not the case. Porosity due to phase separation or reaction with the substrate material can also be ruled out since we find single-phase material in the temperature regime where we observe the porosity and no reaction with the substrate could be observed, see Fig. 2. Dewetting in the liquid state during processing of the films by spray pyrolysis is also not relevant, since porosity should then be found in the as deposited films prior to annealing, which was not the case. Furthermore,

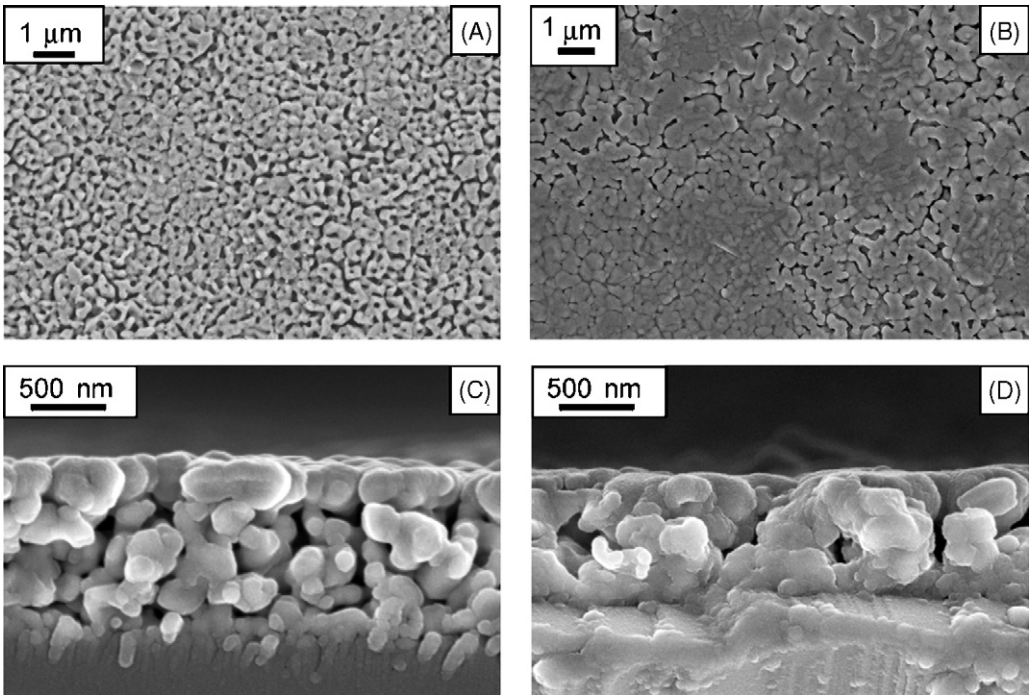

Fig. 9. LSCF films prepared using (A) La, Co, Fe nitrates and Sr chloride, (B) La, Sr, Fe chlorides and Co nitrate, (C) cross-section of (A) and (D) cross-section of (B).

we observe the porosity also in the films fabricated by PLD where no liquid processing step is included.

3.5. Influence of the precursor salt

The amount of porosity can be tailored to some extent by the type of salt used for the precursor. The samples shown in Fig. 5 and the sample shown in Fig. 9(A) and (C) were prepared as defined in Section 2 using nitrate salts except for Sr where chloride was used ("nitrate" sample). As shown in Fig. 9(A) and (C) a porosity of 19% is observed after annealing for 10 h at 1000 °C. The sample shown in Fig. 9(B) and (D) of comparable thickness was prepared using different salts, i.e. chloride salts except for Co where nitrate was used ("chloride" sample). The annealing conditions were the same for both samples. However, in the case of the "chloride" sample, the film is denser; the porosity as determined by SEM is only around 7%.

We attribute the appearance of denser films with the use of more chloride salts to an enhanced densification in the presence of chlorides, as it is known for sintering of calcium hydroxyapatites[46] in the temperature range of our study, although for temperature higher than 900 °C, chlorides lowered the densification.[46,47] Indications that the type of salt influences the porosity are also found for $LiCoO_2$ films. In this case acetates led to higher porosity than nitrates.[48]

We also address the possibility that different decomposition temperatures of the different types of salts might cause the observed porosity as reported by Princivalle et al.,[49] who observed that salts with higher decomposition temperatures led to denser films than those with lower decomposition temperatures. During decomposition of single salts in DTA/TG/MS experiments, we did not find any convincing connection between decomposition temperatures of single salts and film microstructures. During spray pyrolysis the salts will form complexes in the solution and also during the early stage of film formation. The decomposition of these complexes is more important than the decomposition of the single salts as was already shown for CdS[50] and MgO.[51]

3.6. Electrical conductivity

The microstructure of the films also affected their electrical conductivity. The electrical conductivity of samples annealed at different temperatures and prepared from different precursors is shown in Fig. 10. The activation energy for the electrical conductivity calculated between 350 and 600 °C and the porosity of the samples are also shown in this figure. The activation energies of 0.05 eV (sample annealed at 600 °C) to 0.15 eV (samples annealed at 1000 °C) are close to the 0.10 eV found in literature[26] for dense bulk samples between 100 and 500 °C.

The sample annealed at the lowest temperature (600 °C, 4 h) showed the least porosity (2%) and consequently the highest conductivity. When the porosity increased from 2 to 14% (sample annealed at 600 and 800 °C for 4 h, respectively), the conductivity measured at 600 °C decreased from 3170 to 2400 S/m. This is in agreement with equations previously derived for the relation between porosity and conductivity. For a two phase material, consisting of an electrically conductive (LSCF) and a non conductive phase (pores), the effective electrical conductivity σ_{eff} is given by[52]

$$\sigma_{\text{eff}} = \frac{3}{2}\sigma_{\text{LSCF}}\left(1 - \text{Por} - \frac{1}{dim}\right) \quad (2)$$

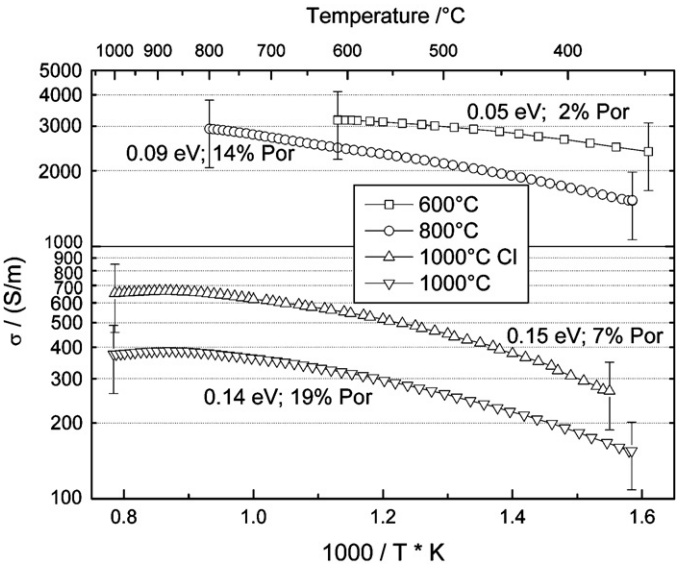

Fig. 10. Electrical conductivity of LSCF films deposited on sapphire annealed for 4 h at 600 and 800 °C and for 10 h at 1000 °C, the less porous film annealed at 1000 °C was prepared using mostly chloride salts. The activation energy for the electrical conductivity calculated between 350 and 600 °C and the porosity of the specimens is also shown.

where Por is the fraction of porosity in the sample and dim the number of dimensions covered by the conductive phase. Since the film thickness is about 5–10 times the grain size, we would consider the conductive phase to be three dimensional. For two samples with different porosity the ratio of the effective electrical conductivity according to Eq. (2) is given by

$$\frac{\sigma_{\text{eff},1}}{\sigma_{\text{eff},2}} = \frac{1 - \text{Por}_1 - 1/\text{dim}}{1 - \text{Por}_2 - 1/\text{dim}} \tag{3}$$

According to Eq. (3), the sample with 14% porosity should have 82% of the conductivity achieved by the sample with 2% porosity. Comparing the values given above, we find that it exhibits 76% of the conductivity. Considering the error bars shown in Fig. 10, the actual results are represented by Eq. (3). The error in determining the conductivity is mainly due to a non-homogenous thickness (see also Fig. 7) of the samples in the measured area (5 mm × 14 mm).

The specimens annealed for 10 h at 1000 °C showed the lowest conductivity. One of these samples was prepared according to the standard parameters given in Section 2 ("nitrate" sample) and one ("chloride" sample) was prepared using mainly chloride salts as precursors except for Co where nitrate was used. The "chloride" sample had fewer pores (7% porosity) and consequently shows a higher conductivity than the "nitrate" sample (19% porosity) when both were annealed at the same temperature. The conductivity of the samples annealed at 1000 °C additionally suffered from the formation of the secondary phases that are detected by XRD analysis. Consequently the conductivity cannot be predicted by Eq. (3) which predicts that the samples should show 92% ("chloride" sample) and 74% ("nitrate" sample) of the conductivity of the sample annealed at 600 °C. However, their conductivity is only 17 and 10% of the sample annealed at 600 °C.

The fact that even for the films exhibiting low porosity the conductivity is lower than for dense bulk samples[53,54] is attributed to the smaller grains and thus more grain boundaries in the thin films and is also confirmed by earlier results[55,56] for similar perovskites with small grain sized microstructures.

4. Summary and conclusion

The preparation of dense LSCF thin films of 100–500 nm thickness with nanosized grains by spray pyrolysis and PLD on different substrates has been shown. These films show solid-state dewetting with pore formation at temperatures higher than 600 °C. At 1000 °C decomposition of this perovskite occurred. The amount of porosity and pore size can be tailored by the annealing temperature and time. The amount of defects in the films probably controls the nucleation of pores. The number of defects is determined by the thin film deposition process. Spray pyrolysis leads to more porosity than PLD for the same annealing conditions. The constraint of the thin film by the rigid substrate during annealing supports pore growth and hinders densification. Further tailoring of the porosity can be achieved by choosing precursors that either support densification (chlorides) or not (e.g. nitrates). The films show semiconductivity in the temperature range from room temperature to 900 °C with a transition to metallic behavior for higher temperatures. The conductivities are one order of magnitude lower than for micron grain sized samples due to the small grain size. Porosity further reduces the conductivity.

The presented results allow engineering of the porosity of LSCF thin films, which allows fabrication of porous thin film cathodes suitable for micro-SOFC.

Acknowledgment

Financial support from Swiss Bundesamt für Energie under the project OneBat – Start and Kommission für Technik und Innovation OneBat Discovery Project and the financial support by the European Union, IP-project REAL-SOFC (SES6-CT-2003-502612) are gratefully acknowledged.

References

1. Barthel, K., Rambert, S. and Siegmann, S., Microstructure and polarization resistance of thermally sprayed composite cathodes for solid oxide fuel cell use. *J Therm Spray Technol*, 2000, **9**, 343–347.
2. Badwal, S. P. S. and Foger, K., Solid oxide electrolyte fuel cell review. *Ceram Int*, 1996, **22**, 257–265.
3. Gauckler, L. J., Beckel, D., Buergler, B., Jud, E., Muecke, U. P., Prestat, M., Rupp, J. and Richter, J., Solid oxide fuel cells: systems and materials. *Chimia*, 2004, **58**, 837–850.
4. Minh, N. Q., Ceramic fuel cells. *J Am Ceram Soc*, 1993, **76**, 563–588.
5. van Herle, J., Ihringer, R., Cavieres, R. V., Constantin, L. and Bucheli, O., Anode supported solid oxide fuel cells with screen-printed cathodes. *J Eur Ceram Soc*, 2001, **21**, 1855–1859.
6. Beckel, D., Muecke, U. P., Gyger, T., Florey, G., Infortuna, A. and Gauckler, L. J., Electrochemical performance of LSCF based thin film cathodes prepared by spray pyrolysis. *Solid State Ionics*, 2007, **178**, 407–415.
7. Beckel, D., Bieberle-Hütter, A., Harvey, A., Infortuna, A., Muecke, U. P., Prestat, M., Rupp, J. L. M. and Gauckler, L. J., Thin films for micro

solid oxide fuel cells. *J Power Sources*, 2007, submitted for publication, doi:10.1016/j.jpowsour.2007.04.070.
8. Huang, H., Nakamura, M., Su, P., Fasching, R., Saito, Y. and Prinz, F. B., High-performance ultrathin solid oxide fuel cells for low-temperature operation. *J Electrochem Soc*, 2007, **154**, B20–B24.
9. Bieberle-Hütter, A., Beckel, D., Muecke, U. P., Rupp, J. L. M., Infortuna, A. and Gauckler, L. J., Micro-solid oxide fuel cells as battery replacements. *Mstnews*, 2005, **04/05**, 12–15.
10. Nikbin, D., Micro SOFCs: why small is beautiful. *Fuel Cell Rev*, 2006, **April/May**, 21–24.
11. Beckel, D., Dubach, A., Studart, A. R. and Gauckler, L. J., Spray Pyrolysis of $La_{0.6}Sr_{0.4}Co_{0.2}Fe_{0.8}O_3$-d thin film cathodes. *J Electroceram*, 2006, **16**, 221–228.
12. Beckel, D., Briand, D., Studart, A. R., de Rooij, N. F. and Gauckler, L. J., Topography mediated patterning of inorganic materials by spray pyrolysis. *Adv Mater*, 2006, **18**, 3105–3108.
13. Muecke, U. P., Messing, G. L. and Gauckler, L. J., The leidenfrost effect during spray pyrolysis of dense NiO-$Ce_{0.8}Gd_{0.2}O_{1.9}$-x thin films. *Thin Solid Films*, 2006, submitted for publication.
14. Muecke, U. P., Luechinger, N. and Gauckler, L. J., Initial status of deposition and film formation during spray pyrolysis of nickel oxide, cerium gadolinium oxide and NiO-CGO thin films. *Thin Solid Films*, 2006, submitted for publication.
15. Rupp, J. L. M., Infortuna, A. and Gauckler, L. J., Microstrain and self-limited grain growth in nanocrystalline ceria ceramics. *Acta Mater*, 2006, **54**, 1721–1730.
16. Perednis, D. and Gauckler, L. J., Thin film deposition using spray pyrolysis. *J Electroceram*, 2005, **14**, 103–111.
17. Perednis, D. and Gauckler, L. J., Solid oxide fuel cells with electrolytes prepared via spray pyrolysis. *Solid State Ionics*, 2004, **166**, 229–239.
18. Willmott, P. R., Deposition of complex multielemental thin films. *Prog Surf Sci*, 2004, **76**, 163–217.
19. Willmott, P. R. and Huber, J. R., Pulsed laser vaporization and deposition. *Rev Mod Phys*, 2000, **72**, 315–328.
20. dos Santos e Lucato, S. L., *Lince—linear intercept v2.4*. Department of Material Science, Darmstadt University of Technology, Darmstadt, Germany, 1999.
21. Beckel, D., Briand, D., Bieberle-Hütter, A., Courbat, J., De Rooij, N. F. and Gauckler, L. J., Micro-hotplates—a platform for micro-solid oxide fuel cells. *J Power Sources*, 2007, **166**, 143–148.
22. Muecke, U. P., Graf, S., Rhyner, U. and Gauckler, L. J., Microstructure and electrical conductivity of nanocrystalline Ni- and NiO-CGO thin films. *Acta Mater*, 2007, submitted for publication.
23. Rupp, J. L. M. and Gauckler, L. J., Microstructures and electrical conductivity of nanocrystalline ceria based thin films. *Solid State Ionics*, 2006, **177**, 2513–2518.
24. Azároff, L. V. and Buerger, M. J., *The powder method in X-ray crystallography*. McGraw-Hill Book Company, New York, Toronto, London, 1958, 46 pp.
25. ten Elshof, J. and Boeijsma, J., Influence of iron content on cell parameters of rhombohedral $La_{0.6}Sr_{0.4}Co_{1-y}Fe_yO_3$. *Powder Diffr*, 1996, **11**, 240–245.
26. Tai, L.-W., Nasrallah, M. M., Anderson, H. U., Sparlin, D. M. and Sehlin, S. R., Structure and electrical properties of $La_{1-x}Sr_xCo_{1-y}Fe_yO_3$. Part 2. The system $La_{1-x}Sr_xCo_{0.2}Fe_{0.8}O_3$. *Solid State Ionics*, 1995, **76**, 273–283.
27. Tai, L.-W., Nasrallah, M. M., Anderson, H. U., Sparlin, D. M. and Sehlin, S. R., Structure and electrical properties of $La_{1-x}Sr_xCo_{1-y}Fe_yO_3$. Part 1. The system $La_{0.8}Sr_{0.2}Co_{1-y}Fe_yO_3$. *Solid State Ionics*, 1995, **76**, 259–271.
28. Bhatt, H. D., Vedula, R., Desu, S. B. and Fralick, G. C., $La_{(1-x)}Sr_xCoO_3$ for thin film thermocouple applications. *Thin Solid Films*, 1999, **350**, 249–257.
29. Lange, F. F. and Kellett, B. J., Thermodynamics of densification. II. Grain growth in porous compacts and relation to densification. *J Am Ceram Soc*, 1989, **72**, 735–741.
30. Jud, E., Huwiler, C. B. and Gauckler, L. J., Grain growth of micron-sized grains in undoped and CoO-doped $Ce_{0.8}Gd_{0.2}O_{1.9}$. *J Ceram Soc Jpn*, 2006, **114**, 963–969.
31. Chen, P.-L. and Chen, I.-W., Grain growth in CeO_2: dopant effects, defect mechanism, and solute drag. *J Am Ceram Soc*, 1996, **79**, 1793–1800.
32. Danielson, D. T., Sparacin, D. K., Michel, J. and Kimerling, L. C., Surface-energy-driven dewetting theory of silicon-on-insulator agglomeration. *J Appl Phys*, 2006, **100**, 083507–083510.
33. Hu, X., Cahill, D. G. and Averback, R. S., Dewetting and nanopattern formation of thin Pt films on SiO[sub 2] induced by ion beam irradiation. *J Appl Phys*, 2001, **89**, 7777–7783.
34. Bolse, T., Elsanousi, A., Paulus, H. and Bolse, W., Dewetting of nickel oxide-films on silicon under swift heavy ion irradiation. *Nucl Instrum Meth Phys Res Sect B*, 2006, **244**, 115–119.
35. Bouville, M., Hu, S., Chen, L.-Q., Chi, D. and Srolovitz, D. J., Phase-field model for grain boundary grooving in multi-component thin films. *Modell Simul Mater Sci Eng*, 2006, **14**, 433–443.
36. Grinfeld, M. A. and Hazzledine, P. M., Rearrangement at coherent interfaces in heterogeneous solids. *Philos Mag Lett*, 1996, **74**, 17–23.
37. Jiran, E. and Thompson, C. V., Capillary instabilities in thin, continuous films. *Thin Solid Films*, 1992, **208**, 23–28.
38. Srolovitz, D. J. and Safran, S. A., Capillary instabilities in thin films. I. Energetics. *J Appl Phys*, 1986, **60**, 247–254.
39. Bolse, T., Paulus, H. and Bolse, W., Swift heavy ion induced dewetting of metal oxide thin films on silicon. *Nucl Instrum Meth Phys Res Sect B*, 2006, **245**, 264–268.
40. Bordia, R. K. and Raj, R., Sintering behavior of ceramic films constrained by a rigid substrate. *J Am Ceram Soc*, 1985, **68**, 287–292.
41. Calata, J. N., Matthys, A. and Lu, G. Q., Constrained-film sintering of cordierite glass-ceramic on silicon substrate. *J Mater Res*, 1998, **13**, 2334–2341.
42. Garino, T. J. and Bowen, H. K., Deposition and sintering of particle films on a rigid substrate. *J Am Ceram Soc*, 1987, **70**, C315–C317.
43. Garino, T. J. and Bowen, H. K., Kinetics of constrained-film sintering. *J Am Ceram Soc*, 1990, **73**, 251–257.
44. Letullier, P. and Heintz, J. M., Elaboration and sintering behavior of a laminar ceramic–ceramic material. *J Phys IV*, 1993, **3**, 1471–1475.
45. Stech, M., Reynders, P. and Rodel, J., Constrained film sintering of nanocrystalline TiO_2. *J Am Ceram Soc*, 2000, **83**, 1889–1896.
46. Nzihou, A., Adhikari, B. and Pfeffer, R., Effect of metal chlorides on the sintering and densification of hydroxyapatite adsorbent. *Ind Eng Chem Res*, 2005, **44**, 1787–1794.
47. Smith, R. M., Zhou, X. D., Huebner, W. and Anderson, H. U., Novel yttrium-stabilized zirconia polymeric precursor for the fabrication of thin films. *J Mater Res*, 2004, **19**, 2708–2713.
48. Chen, C. H., Kelder, E. M. and Schoonman, J., Unique porous $LiCoO_2$ thin layers prepared by electrostatic spray deposition. *J Mater Sci*, 1996, **31**, 5437–5442.
49. Princivalle, A., Perednis, D., Neagu, R. and Djurado, E., Microstructural investigations of nanostructured La(Sr)MnO_3-delta films deposited by electrostatic spray deposition. *Chem Mater*, 2004, **16**, 3733–3739.
50. Krunks, M., Madarasz, J., Hiltunen, L., Mannonen, R., Mellikov, E. and Niinisto, L., Structure and thermal behaviour of dichlorobis(thiourea)cadmium(II), a single-source precursor for CdS thin films. *Acta Chem Scand*, 1997, **51**, 294–301.
51. Stryckmans, O., Segato, T. and Duvigneaud, P. H., Formation of MgO films by ultrasonic spray pyrolysis from beta-Diketonate. *Thin Solid Films*, 1996, **283**, 17–25.
52. Stroud, D., The effective medium approximation: some recent developments. *Superlattices Microstruct*, 1998, **23**, 567–573.
53. Kostogloudis, G. C. and Ftikos, C., Properties of A-site-deficient $La_{0.6}Sr_{0.4}Co_{0.2}Fe_{0.8}O_3$-[delta]-based perovskite oxides. *Solid State Ionics*, 1999, **126**, 143–151.
54. Ullmann, H., Trofimenko, N., Tietz, F., Stover, D. and Ahmad-Khanlou, A., Correlation between thermal expansion and oxide ion transport in mixed conducting perovskite-type oxides for SOFC cathodes. *Solid State Ionics*, 2000, **138**, 79–90.
55. Chen, X., Wu, N. J., Ritums, D. L. and Ignatiev, A., Pulsed laser deposition of conducting porous La–Sr–Co–O films. *Thin Solid Films*, 1999, **342**, 61–66.
56. Furusaki, A., Konno, H. and Furuichi, R., Perovskite-type lanthanum chromium-based oxide-films prepared by ultrasonic spray-pyrolysis. *J Mater Sci*, 1995, **30**, 2829–2834.